Matter and Radiation at Extremes | RESEARCH ARTICLE | scitation.org/journal/mre

Characterization and performance of the Apollon short-focal-area facility following its commissioning at 1 PW level

Cite as: Matter Radiat. Extremes 6, 064402 (2021); doi: 10.1063/5.0065138
Submitted: 30 July 2021 • Accepted: 22 September 2021 •
Published Online: 21 October 2021

K. Burdonov,[1,2,3] A. Fazzini,[1] V. Lelasseux,[1] J. Albrecht,[1] P. Antici,[4] Y. Ayoul,[1] A. Beluze,[1] D. Cavanna,[1] T. Ceccotti,[5] M. Chabanis,[1] A. Chaleil,[6] S. N. Chen,[7] Z. Chen,[4] F. Consoli,[8] M. Cuciuc,[7] X. Davoine,[6] J. P. Delaneau,[1] E. d'Humières,[9] J.-L. Dubois,[9] C. Evrard,[1] E. Filippov,[3,10] A. Freneaux,[1] P. Forestier-Colleoni,[1] L. Gremillet,[6] V. Horny,[1,6] L. Lancia,[1] L. Lecherbourg,[6] N. Lebas,[1] A. Leblanc,[11] W. Ma,[12] L. Martin,[1] F. Negoita,[7] J.-L. Paillard,[1] D. Papadopoulos,[1] F. Perez,[1] S. Pikuz,[10] G. Qi,[12] F. Quéré,[5] L. Ranc,[1,13] P.-A. Söderström,[7] M. Scisciò,[8] S. Sun,[4] S. Vallières,[4] P. Wang,[12] W. Yao,[1,2] F. Mathieu,[1] P. Audebert,[1] and J. Fuchs[1,a)]

AFFILIATIONS

[1]LULI–CNRS, CEA, Sorbonne Université, Ecole Polytechnique, Institut Polytechnique de Paris, F-91128 Palaiseau Cedex, France
[2]Sorbonne Université, Observatoire de Paris, Université PSL, CNRS, LERMA, F-75005 Paris, France
[3]IAP, Russian Academy of Sciences, 603155 Nizhny Novgorod, Russia
[4]INRS-EMT, 1650, Boulevard Lionel-Boulet, Varennes, Québec J3X 1S2, Canada
[5]Université Paris-Saclay, CEA, CNRS, LIDYL, 91191, Gif-sur-Yvette, France
[6]Université Paris-Saclay, CEA, LMCE, 91680 Bruyères-le-Châtel, France
[7]"Horia Hulubei" National Institute for Physics and Nuclear Engineering, 30 Reactorului Street, RO-077125 Bucharest-Magurele, Romania
[8]ENEA, Fusion and Technologies for Nuclear Safety Department, C. R. Frascati, Via E. Fermi 45, 00044 Frascati, Italy
[9]University of Bordeaux, Centre Lasers Intenses et Applications, CNRS, CEA, UMR 5107, F-33405 Talence, France
[10]Joint Institute for High Temperatures, RAS, 125412 Moscow, Russia
[11]Laboratoire d'Optique Appliquée, Ecole Polytechnique–ENSTA–CNRS–Institut Polytechnique de Paris, Palaiseau, France
[12]State Key Laboratory of Nuclear Physics and Technology, School of Physics, CAPT, Peking University, Beijing 100871, China
[13]Laboratoire Charles Fabry, Institut d'Optique Graduate School, CNRS, Université Paris-Saclay, 91127 Palaiseau Cedex, France

[a)]**Author to whom correspondence should be addressed:** julien.fuchs@polytechnique.fr

ABSTRACT

We present the results of the first commissioning phase of the short-focal-length area of the Apollon laser facility (located in Saclay, France), which was performed with the first available laser beam (F2), scaled to a nominal power of 1 PW. Under the conditions that were tested, this beam delivered on-target pulses of 10 J average energy and 24 fs duration. Several diagnostics were fielded to assess the performance of the facility. The on-target focal spot and its spatial stability, the temporal intensity profile prior to the main pulse, and the resulting density gradient formed at the irradiated side of solid targets have been thoroughly characterized, with the goal of helping users design future experiments. Emissions of energetic electrons, ions, and electromagnetic radiation were recorded, showing good laser-to-target coupling efficiency and an overall performance comparable to that of similar international facilities. This will be followed in 2022 by a further commissioning stage at the multi-petawatt level.

I. INTRODUCTION

High-power lasers have become indispensable tools to investigate extreme states of matter subject to ultrastrong electromagnetic fields, enabling a plethora of scientific and technical applications, including the generation of unprecedentedly dense beams of energetic particles, the development of ultrashort and/or ultrabright photon sources, and the laboratory reproduction of high-energy astrophysical phenomena.[1,2]

The Apollon laser system, near completion on the Orme des Merisiers campus in Saclay, France, will be among the first multi-petawatt (PW) user facilities worldwide devoted to studying laser–matter interactions at laser intensities exceeding 2×10^{22} W cm^{-2}. The final goal of the Apollon laser is to generate 10 PW pulses of 150 J energy and 15 fs (FWHM) duration at a repetition rate of 1 shot min^{-1}.[3–5] In its final configuration, the Apollon system will comprise two high-intensity laser beams: F1, with a maximum power of 10 PW, and F2, with a maximum power of 1 PW, which will be simultaneously available to users in both the long- and short-focal areas (LFA and SFA) of the facility. The commissioning of the 1 PW F2 beamline has been completed recently, thus allowing the first laser–plasma interaction experiments to be conducted in both areas.[6,7]

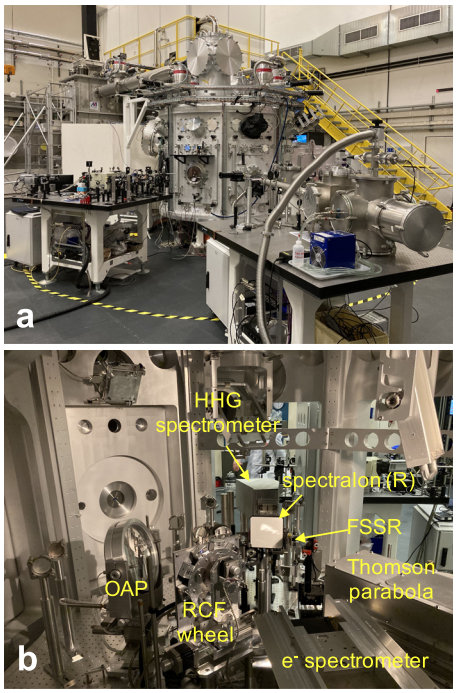

FIG. 1. Photographs of (a) the Apollon SFA and (b) the inside of the vacuum chamber. The off-axis parabola (OAP) that focuses the laser beam onto the target is shown. The various diagnostics used during the experiment are also labeled. The high-order harmonic generation (HHG) diagnostic serves to measure the spectrum of harmonics of the light emitted from the irradiated surface of solid targets. Protons stemming from the (nonirradiated) rear side of the solid targets are detected by a set of radiochromic film (RCF)[11] stacks mounted on a motorized wheel. FSSR is the focusing spectrometer with spatial resolution. The label "R" on the Spectralon plate (a Lambertian scatter plate) stands for "reflection," since this scatter plate allows the (specularly) reflected fraction of the laser beam to be visualized.

In this paper, we report on the current status of the Apollon laser and present the results of the first commissioning experiment that took place in the SFA in May 2021, using the F2 beamline. This experiment was devoted to quantifying the potential of this laser for particle (electron and ion) acceleration and x-ray generation, as well as to characterizing the level of the accompanying electromagnetic pulse (EMP).[8–10]

Figure 1(a) shows an outside view of the vacuum chamber in the SFA, where the F2 beam is focused to high intensity using a low-f-number (f/3) parabola. Figure 1(b) displays the inside of the chamber, together with the equipment fielded during the commissioning campaign.

The remainder of the paper is organized as follows. In Sec. II, we present the parameters of the Apollon PW laser beam. In Sec. III, we give a brief overview of all the diagnostics used for the commissioning campaign and present the physical parameters that could be retrieved from it. In Sec. IV, we discuss the results and draw some conclusions.

II. STATUS OF APOLLON AND ITS F2 BEAM

In the current version of the system, the fifth and final amplification stage (scheduled to provide >250 J pulses in 2022) is temporarily bypassed. Therefore, a maximum pulse energy of 38 J, from the fourth amplifier, can be delivered with a uniform high-quality flat-top beam [see Fig. 2(a)]. The central laser wavelength is $\lambda_L = 815$ nm, with a spectrum extending over 750–880 nm. For the commissioning, we operated the system at a ~30 J pulse energy level with a typical 1.5% rms stability over 6 h of continuous operation. Beam wavefront control was implemented at the output of the amplification section using an adaptive-optics (AO) correction system, consisting of a deformable mirror (DM) with 52 mechanical actuators. A Strehl ratio of ~70%, estimated directly by the focused beam quality, was typically obtained on full energy shots at the output of the amplification section. The 140 mm diameter F2 beam is then directed into the compressor and reaches the target area after about 60 m of free propagation and reflecting off ~30 optical interfaces. A residual wavefront error of ~1.2λ PtV (principally astigmatism) is corrected by manual adjustment of the DM in the amplification section. The resulting beam quality, once focused onto the target by the f/3 focusing parabola [see Fig. 1(b)], is illustrated in Fig. 2(b). The focal spot is recorded by an imaging system positioned after the focus, inside the target chamber. To avoid damage to the imaging system, the fully amplified beam is attenuated before compression and transport to the target chamber. About 41% of the total laser energy is enclosed within a disk of diameter equal to the 2.8 μm FWHM. For a further automatized optimization of the end chain beam, a second AO correction loop on the target will be installed and commissioned in 2022.

Temporal compression is performed by means of a folded compressor composed of two gold gratings (1480 lines mm^{-1}). Pulses of typical 24 fs (FWHM) duration (close to the 23.8 fs Fourier-transform limit) are measured using a Fastlite Wizzler instrument [see the inset in Fig. 2(c)]. The pulse contrast is characterized via different techniques to cover the maximum temporal range. Figure 2(c) displays a third-order cross-correlation measurement conducted at the output of the first Ti:sapphire amplifier, with a a ~ 7×10^{11} dynamic range. A pulse pedestal is clearly observed up to 400 ps before the main peak. A few prepulses are present closer to the peak

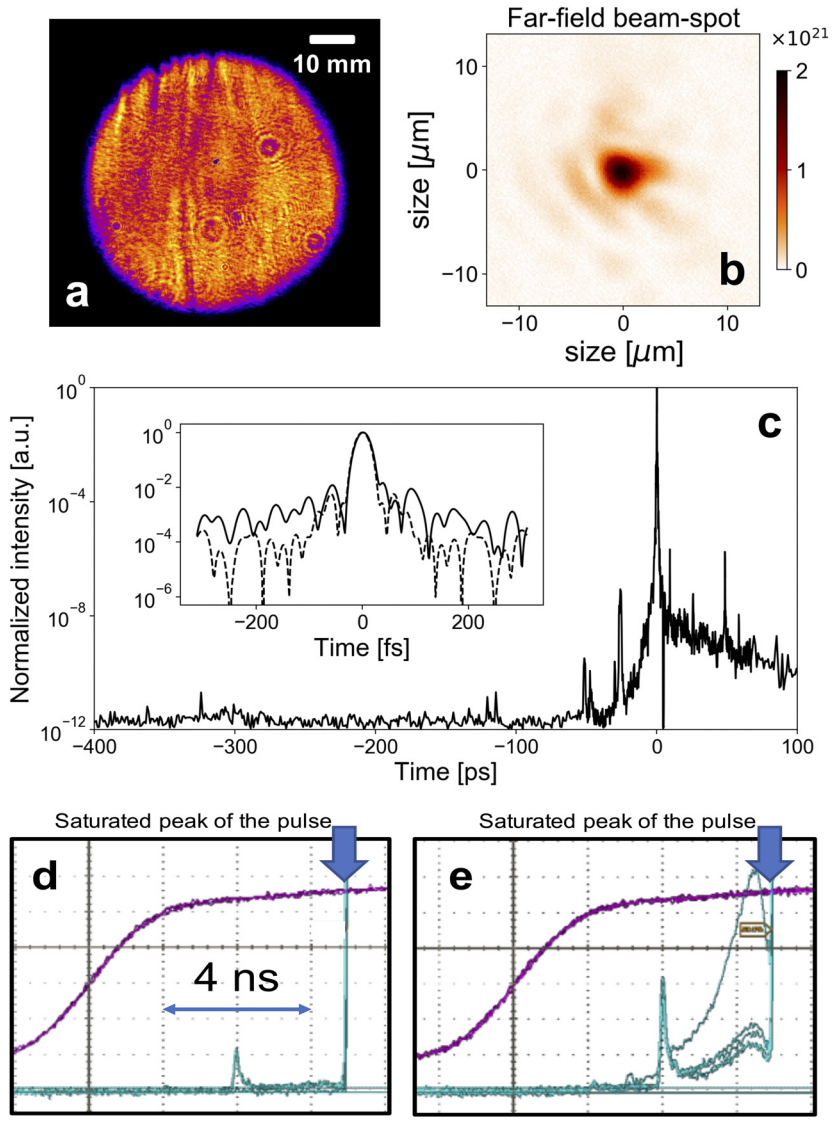

FIG. 2. (a) Near-field beam profile at the output of the fourth amplification stage (out of five in total) operating at 38 J energy level. (b) Full-energy focal spot as measured in the interaction target after high-optical-quality neutral attenuation of the beam before compression. (c) Third-order cross-correlation intensity contrast measurement at the output of the first Ti:sapphire amplifier of the Apollon laser. The inset shows a typical Wizzler measurement of the compressed 24 fs pulses reaching the interaction chamber (solid line). The Fourier-transform-limited (i.e., diffraction-limited) pulse is plotted as a dashed line. (d) and (e) Oscilloscope screenshots showing the pulse contrast measurements using a fast photodiode at the output of the compressor. Two regimes are illustrated: (d) well-adjusted front-end system and nominal operation of the Apollon laser; (e) nonoptimized OPCPA (unstable injection) pump-signal instabilities have an impact on the end chain contrast. In both cases, the main pulse is saturated on purpose in order to see the weak prepulse ahead of it. Note that the peaked prepulse seen at 3 ns in (e) has the same amplitude as in (d). In (e), the vertical scale of the oscilloscope channel has been enlarged to better visualize the unstable behavior of the ASE in the last 3–4 ns before the laser peak. The purple trace in (d) and (e) is the facility trigger.

(especially at −52 and −26 ps), and their origin is under investigation.[12] Figures 2(d) and 2(e) show the temporal intensity profiles as measured at the output of the compressor using a fast photodiode and calibrated optical densities. These single-shot measurements, carried out at full power using a 10 mm subaperture of the beam, have a ~100 ps temporal resolution over a 100 ns timespan. They reveal two salient features. First, an intense prepulse is seen at ~3 ns before the main peak. This particular prepulse, here characterized by an energy contrast of $\sim 10^8$, arises from the on-axis diffusion term of the beam generated by the second amplifier's Ti:sapphire crystal, just before the last pass in the amplifier. Taking account of the laser's low spatial coherence and imperfect compressibility, a conservative estimate of the on-target intensity contrast is $\sim 10^9$–10^{10}. Second, under nominal conditions [see Fig. 2(d)], representing the "good contrast" case, the

amplified spontaneous emission (ASE) noise level is found to lie in the 10^{11}–10^{12} range, in agreement with cross-correlation measurements. However, on-shot measurements exhibit sporadic, yet severe, pulse-to-pulse instabilities of the ASE contrast, in the last 3–4 ns before the laser peak, related to injection instabilities of the front-end (FE) source. These are consequences of optimization procedures of the FE source (performed on a weekly basis) not being strictly applied over the full course of the experimental campaign. This can lead to a rise of almost two orders of magnitude in the ASE level in the last 3–4 ns before the main peak [see Fig. 2(e)], resulting in failed shots. This corresponds to the "poor contrast" case that will be referred to below. The shots performed under these conditions make up about 2%–3% of the total number of shots. Careful monitoring and active correction of these instabilities are expected during the next couple of experimental campaigns.

Given the beam transport losses (~20%) and the compression efficiency (~66%), the maximum energy reaching the interaction chamber is estimated to be ~15 J. Furthermore, when we include the losses due to the uncoated protection silica film of the focusing parabola, the maximum laser energy reaching the target should be of ~10 J. From the recorded focal spot shown in Fig. 2(b), this leads to an on-target peak intensity close to 2×10^{21} W cm^{-2}.

The pointing stability of the focal spot is illustrated in Fig. 3, which displays the transverse motion over time of the beam centroid in the focal plane (at the center of the target chamber). The points were taken every second, using the 10 Hz alignment beam. From it, we can conclude that the beam centroid moves at most by one spot radius.

The back-reflected light from thin foil targets in the SFA is continuously monitored by photodiodes. During the experiment, we observed a relatively high energy level retro-injected in the laser when compared with shooting gas targets in the other experimental area of Apollon, i.e., in the LFA. Unfortunately, we have not yet installed a fully calibrated energy measurement to quantitatively characterize the back-reflected light. However, we can indirectly derive a maximum value for the back-reflection by the absence of damage in the optics of the chain. The front-end of the laser is sufficiently protected from back-reflections by a combination of a Pockels cell and an optical isolator. The most vulnerable part of the system is therefore the first Ti:sapphire amplifier after the FE. Based on our laser system model, taking into account the depletion level of the amplifiers, the timing of the back-reflected light, the beam transport losses, and the laser-induced damage threshold (LIDT) of the optics used, we can safely estimate that the back-reflected light is certainly <500 mJ for 10 J on the target, in other words <5%.

III. RESULTS

A. Setup of experiment and diagnostics

The setup of the commissioning experiment in the SFA area is sketched in Fig. 4(a), with a view of the structure of the breadboard and target manipulator inside the chamber shown in Fig. 4(b). As can be seen in Fig. 4(b), the breadboard is composed of a structure (dark blue) onto which a series of triangular breadboards (turquoise) are inserted. The ensemble is decoupled from the chamber wall, ensuring that whatever is aligned in air moves minimally when the chamber is pumped down. Triangular breadboards allow users to build the setup offline and then directly insert it in the chamber when needed. The same stable structure is also present (but not shown here) above the equatorial plane, allowing diagnostics to be positioned from above the target. The height of the interaction point is 40 cm above the bottom breadboard, and there are 84.5 cm between the interaction point and the roof breadboard. The target manipulator is composed of three linear stages (*xyz*), plus a rotation stage allowing for rotation around the vertical axis.

The targets were held in a rectangular holder having a regular grid structure with holes (of 3 mm diameter). The holder was composed of two parts, the targets themselves (thin foils of various metals or plastic) being held as in a sandwich between the two parts, ensuring planarity. The angle of laser incidence on the targets was 45°, as shown in Fig. 4(a). The laser polarization on target was ~14° relative to the horizontal, i.e., the polarization was close to p-polarization.

To characterize the laser–target interactions, the following diagnostics were used downstream from the target rear: a set of radiochromic film (RCF)[11] stacks on a wheel (which was motorized in and out from the target rear) to diagnose the emitted protons; a

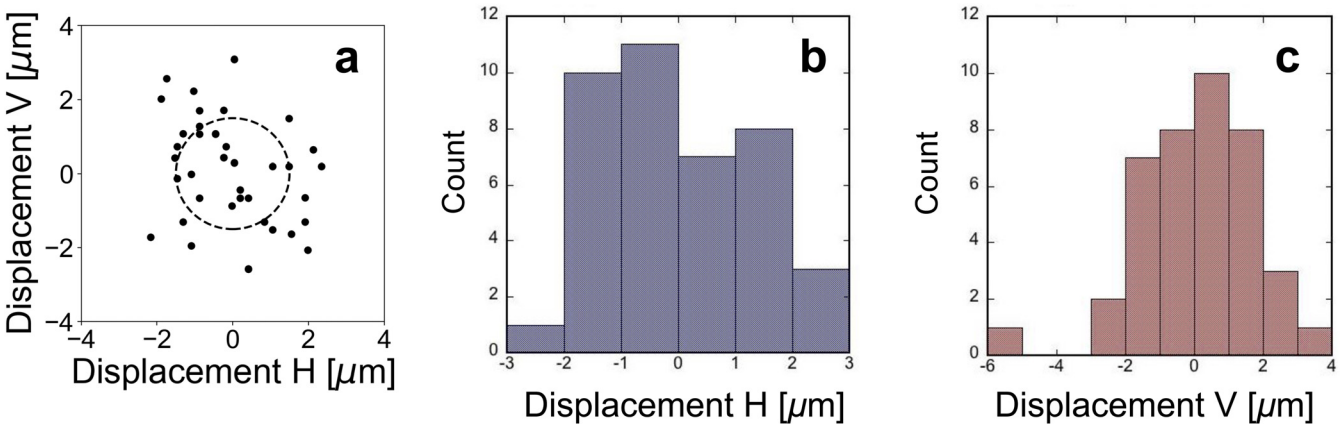

FIG. 3. (a) Laser focus beam-spot centroid motion with time; the dashed circle marks the diameter of the central peak of the laser spot, as can be seen in Fig. 2(b). (b) and (c) Corresponding weighted motion along the horizontal and vertical axes, respectively.

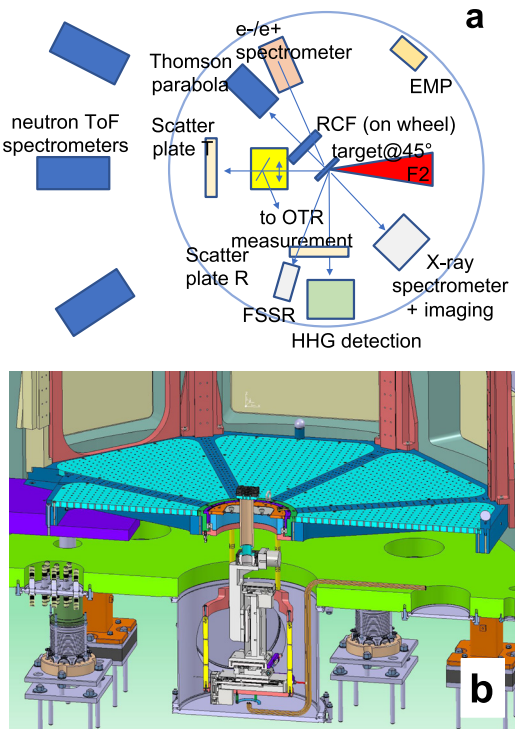

FIG. 4. (a) Top-view schematic of the experimental setup. The red cone represents the focusing cone of the F2 beamline. (b) 3D rendering of the chamber bottom and target positioning system.

Thomson parabola (TP), using CMOS active detectors (acquired remotely) to diagnose the emitted ions; an electron spectrometer, also using CMOS active detectors and coupled with YAG:Ce scintillating crystals to amplify the electron signal (also acquired remotely); a scatter plate at the edge of the TP, allowing us to monitor the transmitted laser energy; an off-axis parabola collecting light, in the axis of the incoming main laser beam, to send it to an optical table outside the chamber to monitor the optical transition radiation (OTR)-generated light by the electrons streaming from the target into vacuum[13] (it was also motorized in and out from the target rear); and a series of neutron time-of-flight base modules to monitor the angular and spectral distribution of the neutrons. The CMOS detectors were RadEye sensors (RadEye1 Large Area Imager, developed by Rad-icon Imaging Corp.), having a 1 × 2 in. detection area, procured from Teledyne DALSA.

Looking at the target, the following diagnostics were used: the laser specular reflection from the target (i.e., at 90° from the incident laser) was diagnosed on a Lambertian scatter plate, which was imaged from outside the target chamber. It allowed us to monitor the reflected laser energy. In the same direction, alternatively to the scatter plate, a high-harmonic generation (HHG) spectrometer was positioned, allowing us to register the x-ray harmonics of the reflected radiation. At angles of 10° and 58° from the target normal, two x-ray spectrometers were positioned, allowing us to record plasma recombination lines. Also at an angle of 10° from the target normal, an x-ray imaging system based on Fresnel zone plates was positioned.

Complementarily, we deployed a set of probes, positioned at various angles around the chamber, inside as well as outside, to measure the electromagnetic pulses (EMPs) generated during the interaction.

The focused laser focal spot [either low-energy from the front-end, or amplified but attenuated before compression; see Fig. 2(b)] was monitored by means of a motorized microscope. The x-ray imaging detailed below provided a complementary full-energy spatial distribution of the laser heating on target.

B. Target alignment

The procedure of target alignment at the target chamber center (TCC) is detailed in Fig. 5. Positioning of the target in the focal plane

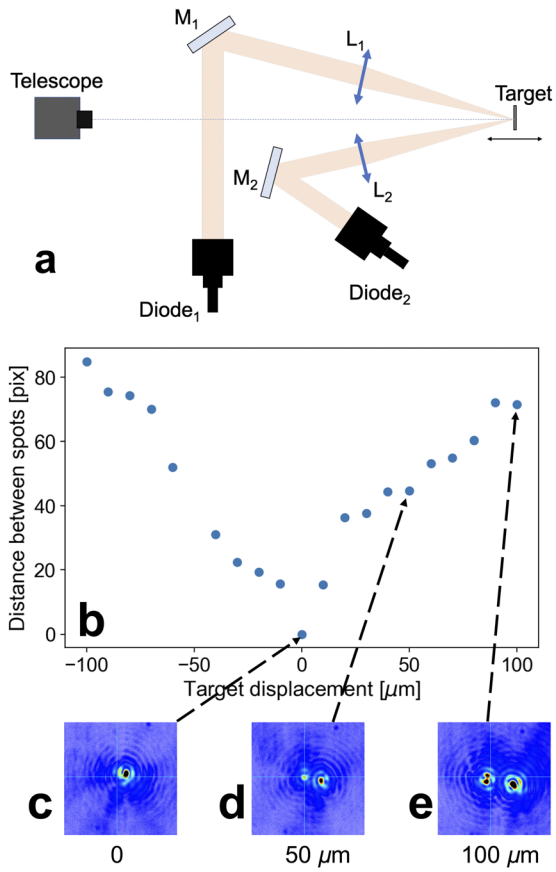

FIG. 5. (a) Target alignment procedure: the alignment beams produced by laser diodes coupled to beam expanders ($Diode_1$ and $Diode_2$) are transported inside the vacuum chamber by 100% reflective mirrors (M_1 and M_2) and are focused on the same point in space [the target chamber center (TCC), which is position 0 in (b)] by means of lenses (L_1 and L_2). The target can be adjusted in focus, i.e., back and forth along the main laser axis. The telescope, which is positioned outside the chamber, looks at the surface of the target with a high magnification. By scanning the target along the focus axis, we can observe that the two spots of the alignment beams are either overlapped [as in (c)] or separated [as in (d) and (e)]. The distance between the two spots depends on the target displacement from TCC, as shown in (b), where a positive direction corresponds to the target moving toward the laser-focusing OAP.

of the laser was performed using two converging continuous-wave (CW) laser beams, delivered by two laser diodes coupled with beam expanders. Prior to the positioning of a target at the TCC, each alignment beam was focused by a lens to the TCC point, which was materialized by the top of a wire, which was itself observed by two telescopes (from Questar Corp.) positioned in air on the chamber walls, one looking down on the target over the main laser axis, the other located at 90° from the first one.

When the target surface was placed at the TCC, the telescope looking at the target above the main laser axis registered one tiny intense bright spot, as shown in Fig. 5(c). Moving the target back and forth led to divergence of the beam spots from the two alignment lasers, with a reduction in their intensity and an increase in their size, as shown in Figs. 5(d) and 5(e). As can be seen in Fig. 5(b), this procedure allowed each target to be easily positioned with a ±20 μm precision, i.e., within the Rayleigh length of the main laser beam.

C. Scattered laser light from the target

The scattered light in the direction of laser propagation and in the direction of specular reflection from the target surface was measured using Spectralon scatter plates and imaged by Basler CMOS cameras positioned in air on the chamber wall [see Fig. 4(a)].

Figure 6 shows the spatial distributions of the second harmonic (2ω = 408 nm) of the scattered light (which was selected using a bandwidth color filter) reflected from the target. It is clearly seen that with good laser contrast [see Fig. 2(d)], the shape of the reflected beam has a similar topology to that of the laser near field, demonstrating a quasi-mirror-like plasma surface, whereas with a poor laser contrast [see Fig. 2(e)], the laser beam becomes divergent and becomes widely scattered after having irradiated the target.

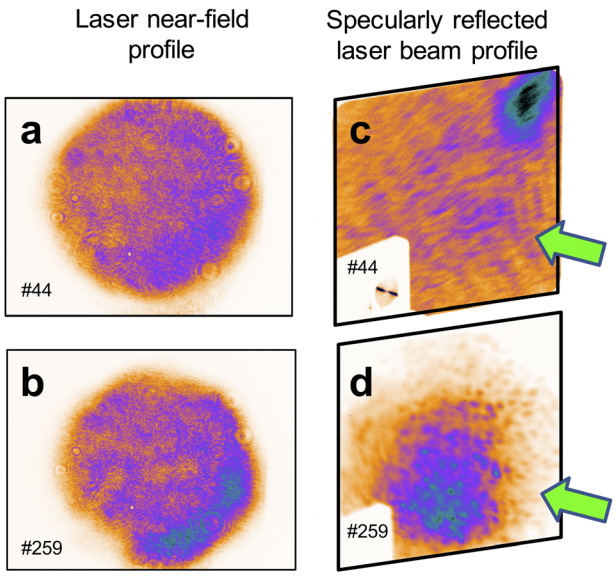

FIG. 6. (a) and (b) Laser near-field images, captured after full amplification and before compression. (c) and (d) Images, captured by an imaging camera positioned outside the chamber, of the specularly reflected laser beam landing on the Spectralon plate after having irradiated (c) 10 μm and (d) 3 μm thick Al targets. The green arrow indicates the direction of laser propagation. The white rectangle in the bottom left of the images is the shadow of an object positioned between the target and the scatter plate, partially blocking the light on its way to the scatter plate. The top row shows poor contrast conditions and the bottom row good contrast conditions.

D. Self x-ray emission

Three diagnostics, all looking at the target front, were implemented to characterize the laser–solid interactions in the soft x-ray domain.

First, a Fresnel ultra-high-resolution imager (FUHRI)[14] recorded the target self-emission at an angle of 10° from the target normal

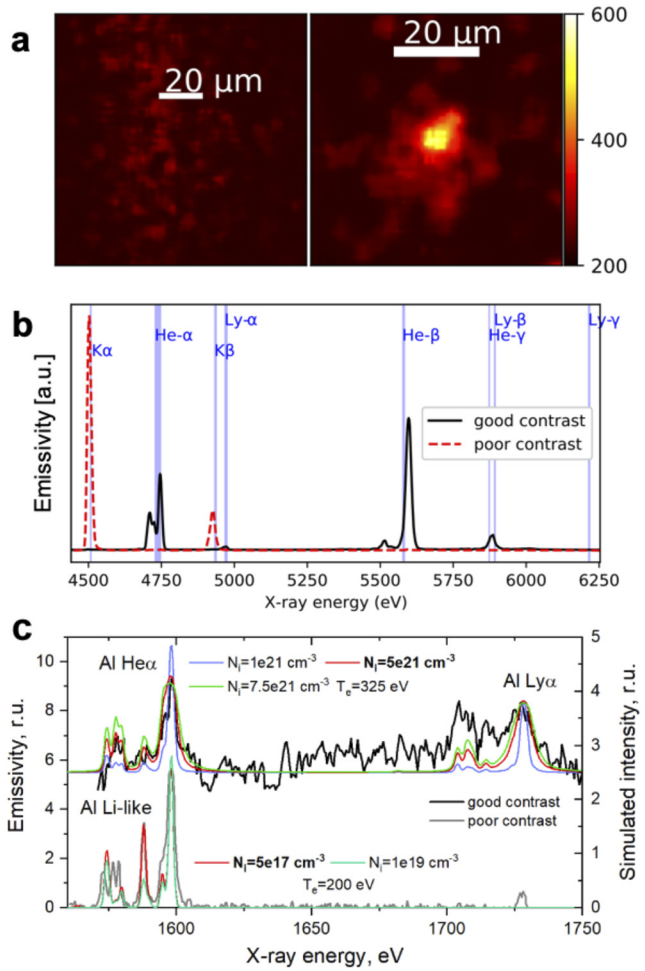

FIG. 7. Self-emission x-ray signals from the target front surface. (a) Images from (left) a Ti target, with poor laser contrast, and (right) an Al target, with good laser contrast. (b) Spectra from a thin Ti layer buried between plastic layers. (c) Al spectra obtained using the FSSR spectrometer, together with simulations performed using the PrismSPECT code. The simulated spectra are normalized to the experimental ones using the intensities of the Ly_α and He_α lines. The offset in energy between the spectra obtained under good and poor contrast conditions is artificial and is plotted this way to allow comparison of the two spectra.

in the x-ray range 4.7 ± 0.1 keV. This diagnostic consists of a Fresnel zone plate of focal length ~250 mm set with a magnification of 15.5, a multilayer mirror acting as a monochromator, and a CCD camera as a detector. The spatial resolution was previously measured to be between 3 and 5 μm. Figure 7(a) illustrates typical results from this imager, highlighting the strong difference made by poor laser contrast. The <10 μm spot of the right-hand panel corresponds to continuum emission from the oscillating electrons in the laser focal spot, or from their bremsstrahlung emission, confirming the proper focusing of the laser.

The second instrument provided x-ray spectra in the Ti K-shell range (4.4–6.3 keV)[15] at an angle of 10° from target normal. It consists of polycapillary x-ray optics able to collimate x-rays over a few meters up to a curved Bragg crystal that disperses the signal on a CCD camera. This setup allows for an active detector far away from the target in order to reduce the impact of the EMP, while keeping a good spectral resolution of $E/\Delta E \sim 1000$. A typical spectrum, from a 200 nm Ti layer buried between two 2 μm thick layers of plastic, is provided in Fig. 7(b). It can be observed that in the case of poor contrast, fast electrons accelerated by the laser in the preplasma traverse the Ti layer, inducing K_α emission, characteristic of a weakly ionized cold plasma. It is indeed expected that a large preplasma prevents efficient coupling between the hot electrons and the target bulk. In the case of good contrast, the preplasma remains limited, and the spectrum shows thermal emission from the hot Ti layer (He-like and H-like ions). This indicates that the temperature reached above 1 keV in the buried layer, i.e., close to solid density. Precise atomic calculations will be carried out to interpret these results with more accuracy.

The third diagnostic was a focusing x-ray spectrometer with spatial resolution (FSSR).[16] It was used to record the emission of the plasma at the front surface of the target in the soft x-ray domain in a narrow spectral range from 1.5 to 1.8 keV. The spectrometer was installed at a direction of 70° to the target normal and 10° down from the equatorial plane in order to avoid self-absorption of x-ray emission in the plasma plume and to reduce the parasitic fluorescence of the spectrometer crystal caused by hot-electron flows. Figure 7(c) compares x-ray spectra of Al as obtained under poor and good contrast conditions (black and grey curves). H-like and He-like spectral lines are observed in this range, with their satellites. X-ray spectra with good and poor contrast were simulated by the radiative-collisional code PrismSPECT, taking into account an optical thickness that is equivalent to the measured focal size (3 μm). The simulation was done to fit the intensity ratios between the He_α line, its Li-like satellites, and the Ly_α line, as well as the widths of the He_α and Ly_α lines. The text in bold font in Fig. 7(c) describes the parameters of the best fit of the simulation with respect to the experimental spectrum. The satellites of the Ly_α line are supposed to be generated by radiative pumping, which is not included in the model. As we can see in Fig. 7(c), when the laser temporal contrast is good, we observe an increased mean ionization charge (i.e., a larger ratio between the Ly_α and He_α lines) as well as broadened lines due to higher thermal electron temperature and density.[17,18] Compared with the case of poor laser contrast, we observe that in the case of good laser contrast, the ion density is increased by four orders of magnitude, up to $\sim 5 \times 10^{21}$ cm^{-3}. The electron temperature is increased as well, from 200 to 325 eV. The spectra were recorded by an x-ray CCD camera (Andor DV430), as well as by conventional image plates. Note that under poor contrast conditions, no clear continuum emission signal from the fast electrons could be obtained, which concurs with the idea that these did not encounter much dense matter. Conversely, with good contrast, the spectrum shows a significant continuum (here subtracted from the spectrum), thus supporting the idea that the solid target was then mainly intact at the time of the high-intensity irradiation, allowing fast electrons to penetrate the solid region and produce bremsstrahlung.

E. High-order harmonic generation

A high-order harmonic spectrometer coupled with a microchannel plate (MCP) detector was placed in the direction of specular light reflection from the target surface.

Figure 8 presents one spectrum of high-order harmonics of the laser pulse obtained during the experiment. The obtained high-harmonic spectrum extends to the 17th harmonic, i.e., to a wavelength of ~50 nm. The laser energy in the pulse was ~10 J, and the target was a 3 μm thick Al foil. The spectrometer is based on a extreme ultraviolet (XUV) grating of 1200 grooves mm^{-1} from Hitachi and a microchannel plate (MCP) detector. As illustrated in Fig. 8(a), the harmonic beam is angularly resolved. Note that the angular window on which the beam is observed is limited by the grating width, approximately between −30 and 30 mrad here. Owing to this limitation, the harmonic beam divergence could not be evaluated.

There are two HHG regimes when a laser is reflected from a plasma mirror,[19,20] namely, the coherent wake emission (CWE) and relativistic oscillating mirror (ROM) regimes, each occurring under very different physical conditions. The CWE regime is predominant when the plasma gradient at the target surface is shorter than $\lambda_L/20$ (where λ_L is the laser wavelength) and when the laser intensity on target is not relativistic ($I < 10^{18}$ W cm^{-2}), whereas the ROM regime is predominant when the plasma gradient scale-length is longer, between $\lambda_L/20$ and $\lambda_L/5$, and with relativistic laser intensity on target, i.e., when $I > 10^{18}$ W cm^{-2}, such that the electrons are driven to near the speed of light.[21]

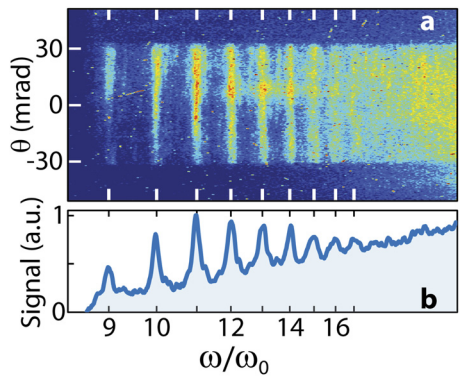

FIG. 8. High-order harmonic spectrum measured during the commissioning experiment, using the F2 beamline of Apollon. The XUV beam in the specular axis resolved spectrally from ~90 to ~10 nm and, as can be seen in (a), resolved angularly in the range −30 to 30 mrad. (a) Raw image measured by imaging the MCP detector with a camera. (b) Angularly integrated signal between −10 and 10 mrad.

The harmonic spectrum observed in Fig. 8 most likely results from the ROM mechanism, since the on-target laser intensity is evaluated to be ~2×10^{21} W cm^{-2}, and no prior plasma mirror was used to improve the laser temporal contrast.[22] Thus, a relatively extended preplasma is expected to be generated by the laser pedestal. Note that driving HHG on solid targets without using a plasma mirror is extremely challenging, owing to the constraints imposed on the temporal contrast of the laser system; this statement holds even at 100 TW-class laser facilities. The fact that we can observe HHG therefore demonstrates the excellent contrast of the laser system, consistent with other measurements.

F. Proton acceleration

The proton beam accelerated from the target backside was characterized in energy and angle using a combination of widely accepted methods, namely an RCF stack[23] and a Thomson parabola spectrometer.[24] We used various target materials (plastic and metal) of thicknesses decreasing from 30 μm down to 0.8 μm. Such a thickness scan is a standard procedure to quantify the actual prepulse level on target.[25–27] Indeed, for relatively thick targets as explored here, target normal sheath acceleration (TNSA) is expected to be the dominant ion acceleration process,[28–31] with well-assessed characteristics (acceleration along the target normal, known scaling with laser intensity, and known variation of beam divergence with energy). For this commissioning experiment, we focused only on an acceleration regime governed by TNSA, to be able to compare our results with the extensive collection of experimental data on TNSA gathered over the past two decades.

Reducing the target thickness first tends to enhance the proton energies since the sheath field set up at the backside by the widely divergent hot electrons[32,33] is strengthened. If the target is made too thin, however, its rear surface may prematurely expand owing to thermal or shock waves induced by the laser pedestal. The long density gradient thereby formed at the target rear is detrimental to proton acceleration.[34] The target thickness maximizing proton acceleration is therefore a good indicator of the on-target prepulse level.

We also tested double-layer targets during this campaign, namely, carbon nanotube foams (CNFs) deposited on Al foils. The CNFs were fabricated using an improved floating catalyst chemical vapor deposition method.[35] The thickness of the Al foils was set to 15 μm, and the thickness of the CNFs ranged from 20 to 80 μm. The density of the CNF was 2.6 ± 0.3 mg cm^{-3}, corresponding to an electron density of $(0.45 \pm 0.05) n_c$ at full ionization ($n_c = m_e \omega_L^2 \epsilon_0 / e^2$ is the critical density of the plasma at the laser frequency $\omega_L = 2\pi c/\lambda_L$). These yielded results (not detailed here) similar to those obtained with plain foils.

The motorized RCF stack holder was made on the basis of the revolver/carousel principle. In this technique, a series of RCF stacks are positioned on the periphery of a rotating disk. A lead screen protects the stacks from radiation emitted by the target, except for one slot, corresponding to the stack positioned just behind the target. After a shot is completed, the exposed stack is rotated behind the screen, while a fresh, so far unexposed, stack is positioned behind the new target. The rotation is motorized, so that the changing of stacks between shots can be done remotely, without access to the chamber [see Fig. 1(b)]. The stacks in our experiment used RCFs of type HD-v2 and EBT3,[36] with various filters composed of polyethylene in order to set a desirable range of energies.

We conceived the electron/Thomson parabola spectrometer ANNA ("Apollon Thomson parabola") as being tailored to the needs of particle acceleration experiments at Apollon. Having passed through an entrance pinhole (whose diameter may range between 50 μm and 1 mm), particles are dispersed by a 1.1 T magnetic field [produced by 70 mm diameter round magnets; see Fig. 1(a)] and deflected by an electric field between two copper slabs whose voltage difference can be a maximum of 10 kV. An optimal combination of pinhole diameter, voltage difference, and geometrical shape of the slabs allows us to record the entire proton spectral distribution between 1 and 100 MeV. Three different backs have been designed in order to collect (protons and) ions on a film detector (Image Plate or CR-39), an MCP, or a CMOS detector. Moreover, the electron spectral distribution between 4 and 100 MeV can optionally be obtained by collecting the fluorescence of calibrated YAG:Ce crystals placed on one side of ANNA (normal to the ion detection plane) and imaged by a camera. ANNA was positioned along the target normal, with its front pinhole at a distance of 320 mm from the TCC and with a pinhole of 200 μm diameter. The electrodes were charged at ±2 kV. To operate in high-repetition mode, the TP detector was composed of two highly sensitive RadEye CMOS matrices mounted head to tail. Protons impacted the CMOS surface directly. Figure 9(a) presents a schematic top view of the spectrometer, and Fig. 9(b) shows the mounting and cabling of the CMOS detectors inside the TP assembly; an additional cover was added on top of what is shown in the photograph so that the detectors were enclosed in a Faraday cage to avoid electromagnetic perturbations onto the readout system. A detailed calibration of the instrument and of the CMOS detectors was performed, but since it is outside the scope of this report, it will be described elsewhere.

The CMOS detectors were triggered 1 ms before the shot and read out immediately after. The signal was acquired remotely after

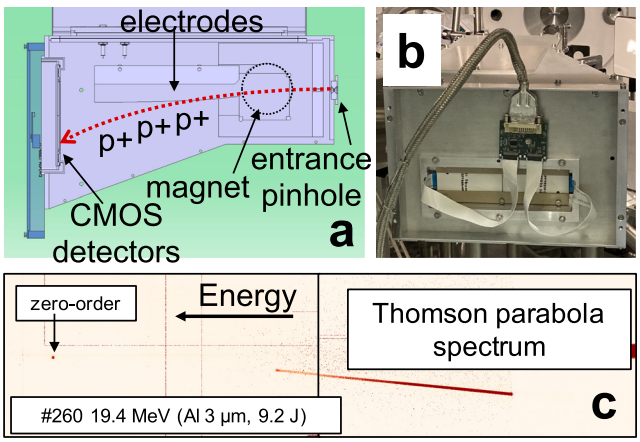

FIG. 9. (a) Schematic top view of Thomson parabola (TP). (b) Photograph of the back view with RadEye CMOS detectors. (c) Typical spectral image obtained in a single shot with the TP. One can clearly see the boundary between the two CMOS detectors that are mounted head to tail. The low-energy part of the spectrum has been intentionally cut by a thick Al filter, because it saturated the detector, since the number of particles increases exponentially toward low energies.

each shot, thereby allowing us to use the TP continuously over a series of shots without the need to access the detector, as is the case when employing commonly used imaging plates,[37] which imposes the need to break the vacuum of the target chamber to read them out.

Figure 9(c) shows a typical proton spectrum, with a 19.4 MeV cutoff energy, emitted from a 3 μm Al target irradiated with an on-target pulse energy of 9.2 J, as registered by the TP spectrometer. The measurement consists of two separated images collected by the two RadEye CMOS matrices. The so-called zero-order is the point-projection of the neutral atoms and x-rays emitted by the target onto the detector. It serves as a reference from which the deflection of the charged particles can be accounted for. A track of deflected protons can be seen on the right-hand side of the image, with a high-energy cutoff and a broad spectrum, both of which are typical signatures of TNSA.[29] The proton track is parabolically curved, as is expected.[24]

We have been able to generate proton beams with maximum cutoff energy around 28 MeV from 2 to 3 μm thick Al foils, consistent with results obtained at other facilities under similar experimental conditions.[27,38]

Figure 10 plots the variations in the proton cutoff energy with Al foil thickness, as recorded by the RCF and TP diagnostics. Black dots for RCF and red triangles for TP represent the averaged proton cutoff values over several shots, and the vertical lines marks the range of the recorded cutoff energy values over these shots.

The proton cutoff energies recorded by the RCFs appear to be higher than those diagnosed by the TP for 1.5 and 3 μm target thicknesses. This is due to deflection of the proton beam, as observed on the RCFs. The higher-energy portion of the proton beam turned out to deviate from the target normal direction and therefore was not collected by the TP. This phenomenon can result from a hybrid acceleration mechanism, as proposed in Ref. 39, but under quite distinct interaction conditions. A more thorough analysis is thus needed to interpret our data, and this will be the subject of a separate paper.

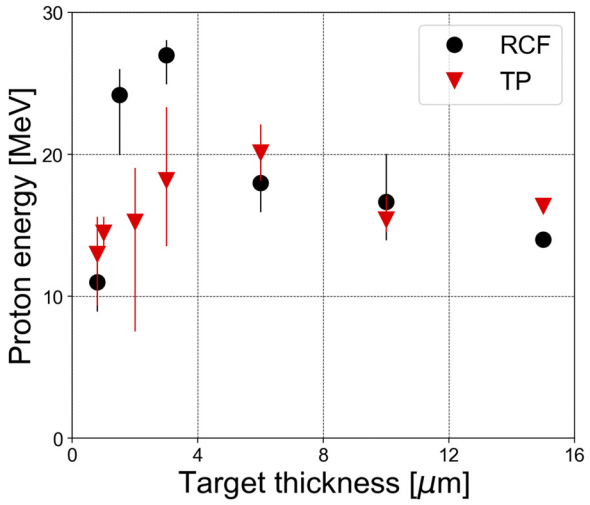

FIG. 10. Maximum proton energies, as registered by RCFs and Thomson parabola, depending on the target thickness. The targets are plain Al foils.

G. Hot-electron generation

The electron spectrometer was placed with its entrance pinhole at 440 mm from the TCC, along the axis perpendicular to the target surface, alternatively to the TP. The entrance pinhole diameter was 1 mm. The spectrometer held a pair of magnets that created a magnetic field of 1 T to disperse the incoming electrons in space, with energy from 3 to 50 MeV.

The detector of the spectrometer was composed of four RadEye CMOS detectors, as shown in Fig. 11(a), which were installed at an angle to maximize the use of the detector and to accommodate the fixed position of the electronic board. A 1 mm thick YAG:Ce scintillating crystal was set flush onto the detectors to convert the incoming electron signal into visible light at a central wavelength of 550 nm [see Fig. 11(a)]. Like the TP diagnostic, the electron spectrometer was used without the need to break vacuum, i.e., the RadEye signal was read remotely after every shot.

To have an absolute calibration of the electron deposition on the CMOS, for one shot we placed a grid made of an image plate with a known response to the electron impact[40] in front of the YAG:Ce scintillator, as can be seen in Fig. 11(a). A detailed review of the absolute calibration of the RadEye CMOS coupled with a YAG:Ce crystal will be the subject of a separate technical publication.

The raw signal registered by the RadEye is presented in Fig. 11(b), and the extracted electron spectrum is shown in Fig. 11(c).

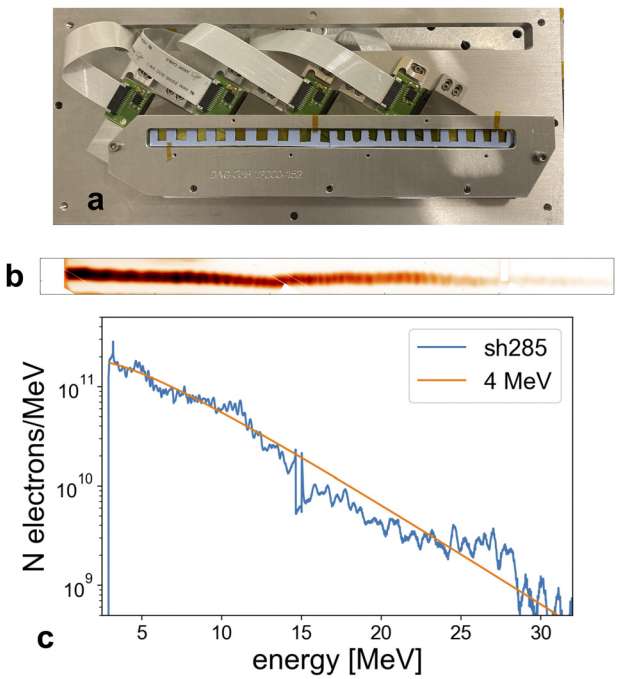

FIG. 11. (a) Photograph of the lateral panel of the electron spectrometer detector assembly, showing how the RadEye CMOS detectors are mounted on it. (b) Raw image of a recorded electron spectrum from a composite 20 nm Al + 23 μm polyethylene terephthalate (PET) target. For this particular shot, the distance from the TCC to the spectrometer entrance was 290 mm. (c) Hot-electron spectrum retrieved from the raw image [shown in (b)] and the corresponding Maxwellian distribution fit using an energy of 4 MeV.

H. Neutron generation

The spectra of neutrons produced by converting the accelerated protons into a converter (Li or Pb)[41] were diagnosed with an array of time-of-flight modules positioned outside the target chamber [see Fig. 4(a)]. These were EJ-254 modules with a 1% loading of boron scintillator rods, coupled at both ends of the rods to two photomultiplier tubes (PMTs), and they ran in coincidence counting mode. These modules have been shown to perform well in high-power laser electromagnetic environments.[42] The diagnostic looked at the target at various angles. An example of such a measurement is shown in Fig. 12. A detailed analysis of the signals is underway and will be reported separately.

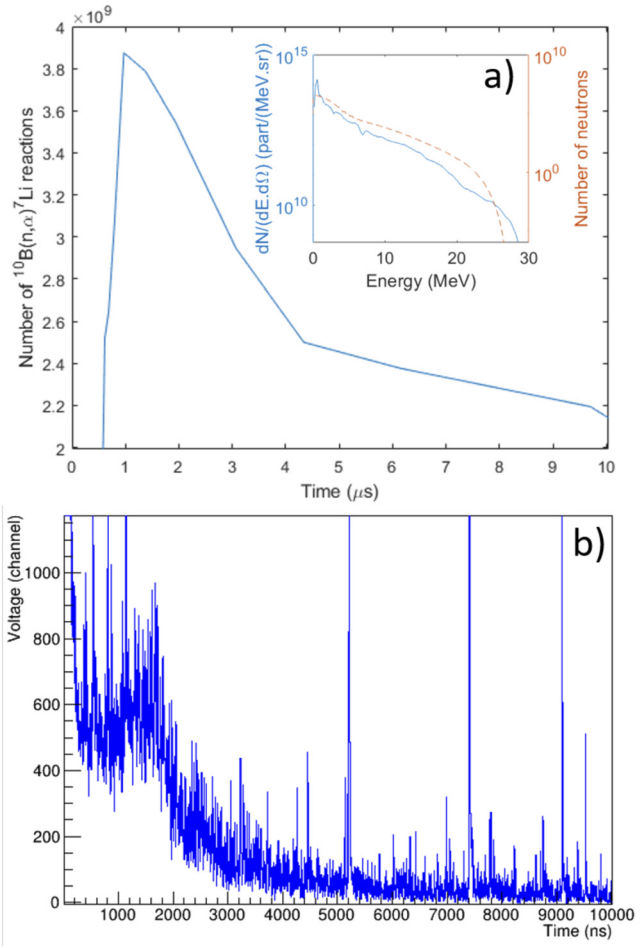

FIG. 12. (a) Predicted number of events (as a function of time) produced in a boron-doped plastic scintillator of type EJ-254, placed at 6 m from the target, when exposed to the neutron spectrum shown by the dashed line in the inset. That neutron spectrum results from having a proton beam with maximum energy 28 MeV, also shown in the inset (full line) irradiating a Pb converter. The neutron generation in Pb is simulated using GEANT4. The events in the scintillator are simulated using the known cross-section in 10B (which decreases strongly when the incoming neutron energy increases), and the neutron spectrum (dashed line shown in the inset): starting at $t = 0$, there are no events, because there are no neutrons that have yet flown to the detector. As the neutron spectrum peaks around 1 MeV, and decreases for lower energies, this results in the events having a peak around 1 μs. (b) Actual time-of-flight chronogram recorded during the commissioning experiment, from a proton beam with maximum energy 28 MeV impinging on a 1 mm thick Pb converter. The signal is high at $t = 0$ owing to the gamma flash and the EMP. However, we notice a clear "bump" located at ~1.5 μs, akin to what is expected based on the calculation shown in (a).

I. Optical transition radiation

A diagnostic of the coherent optical transition radiation (OTR) emitted by the hot electrons when they cross the rear side of the solid target toward vacuum[13] was also implemented in the experimental setup. The particular interest of this diagnostic is that it can be used to image electron generation at full power and thus constitutes essentially a monitor of the intensity distribution of the high-power laser focal spot.

The OTR light was collected by means of an off-axis parabolic mirror ($f/6$), placed on the same axis as the main laser beam and 150 mm downstream from the target (see Fig. 4). The light originating from the target was collimated by the parabola and transported from the vacuum chamber to an optical table, where it was analyzed by a set of Andor cameras. These registered the spatial distribution of the radiation at the fundamental (1ω = 815 nm) and second-harmonic (2ω = 408 nm) wavelengths of the laser. The cameras imaged the plane of the target positioned at the TCC. Additionally, another Andor camera coupled with a spectrometer was also used, allowing us to register the spectral components of OTR harmonics. To prevent the collection OAP mirror from damage, it was protected by a neutral optical density filter.

Figure 13 demonstrates the raw spatial distribution of the OTR as recorded at the fundamental laser harmonic, registered while irradiating a 2 μm thick Al target. The beam-spot shape is well reproducible from shot to shot. It basically shows that the zone from which the hot electrons are generated is narrow and well localized. A detailed analysis of the OTR results will be the subject of a separate work.

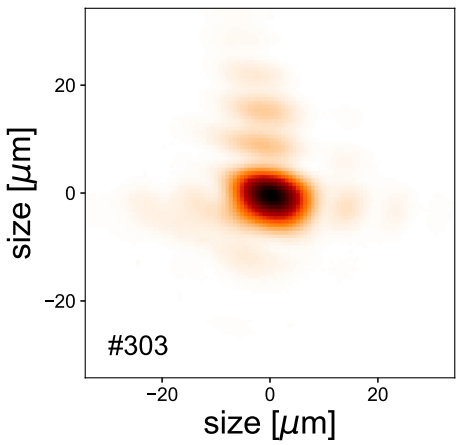

FIG. 13. OTR image collected at 1ω and emitted from the rear side of a 2 μm thick Al target. The image is larger than that of the focal spot shown in Fig. 2(b) owing to the intrinsic limited resolution of the $f/6$ imaging parabola.

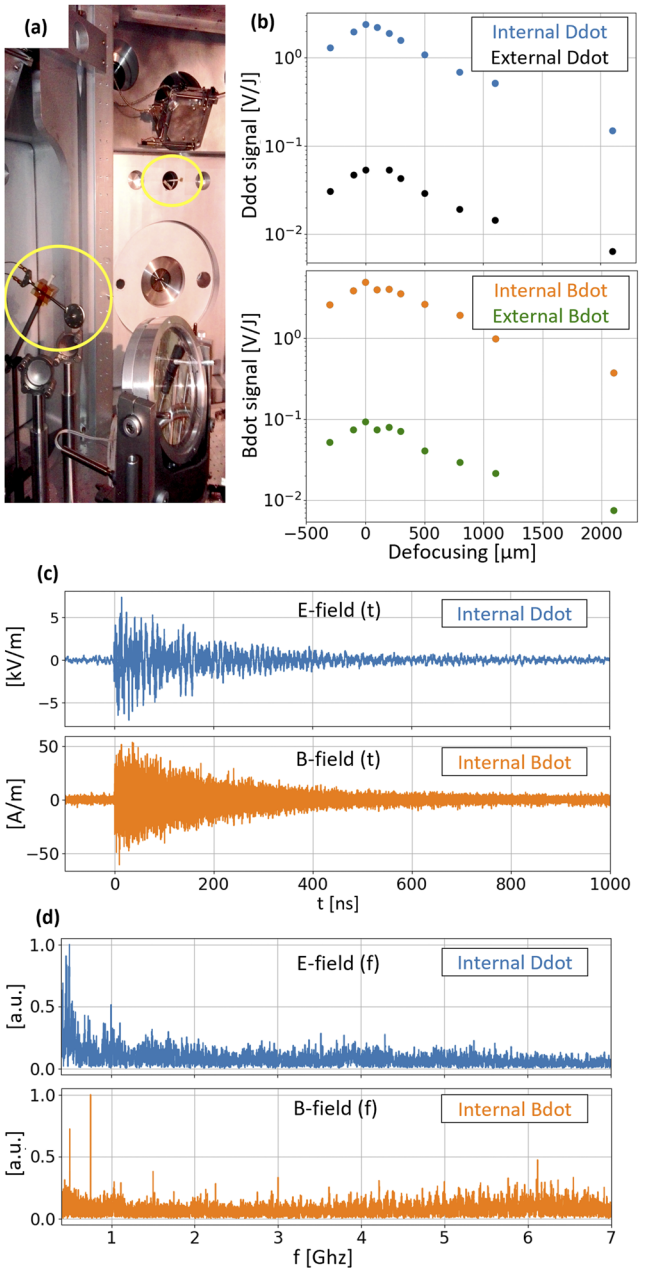

FIG. 14. (a) Photograph of the electromagnetic field probes inside the target chamber: the D-dot probe is on the left behind the focusing parabola, and the B-dot probe is on the right. (b) Amplitude of the raw signals (expressed in volts and normalized to the laser energy) as a function of the laser focusing position on target (a motion in the positive direction means that the focusing parabola was moved closer to the target). (c) Temporal evolution of the electric (blue, D-dot) and magnetic (orange, B-dot) fields inside the target chamber. (d) Frequency spectra of the electric and magnetic fields displayed in (c).

J. Electromagnetic pulse generation

Monitoring the levels of electromagnetic pulses (EMPs) is of paramount importance for the development of high-power, high-energy laser facilities.[8–10] These transient electromagnetic fields in the radiofrequency–microwave range (MHz to tens of GHz) can reach remarkable intensities (beyond the MV m^{-1} level close to and up to ~1 m away from the TCC) that scale with laser energy and mostly with laser intensity at focus,[9] and for this reason can be a source of fatal damage or failure of electrical equipment. On the other hand, they may represent an interesting diagnostic tool for laser–plasma interaction, since the intensity and the temporal and spectral features of the related electric and magnetic fields can be correlated with the specific interaction conditions of each shot series of the experimental campaign. Detecting the laser-generated EMP radiation is thus of primary importance.

For this purpose, the Apollon facility has been equipped with an EMP measurement platform consisting of the following elements:

(i) two D-dot probes: Prodyn AD-80D(R) differential electric field sensors;[9,43]
(ii) two B-dot probes: Prodyn RB-230 differential magnetic field sensors;[9,44]
(iii) a balun (Prodyn B170) associated with each probe, for differential signal detection and rejection of common-mode signals;[9,45]
(iv) a suitable set of semirigid, double-shielded cables;
(v) a high-performance Faraday cage: Siepel (French supplier) with attenuation >100 dB from 30 MHz to 6 GHz;
(vi) an oscilloscope: Agilent Infinium 90804A (four channels, 8 GHz).

In this commissioning campaign, one D-dot probe was placed inside the chamber at a distance of ~65 cm from the TCC and behind the focusing parabola, which acted as a suitable shield for direct particles and ionizing electromagnetic radiation coming from the plasma, as shown in Fig. 14(a). A second D-dot probe was placed outside the chamber at a distance of ~370 cm from the TCC. Similarly, one B-dot probe was placed inside the chamber [see Fig. 14(a)] at a distance of ~100 cm from the TCC and shielded by a black Al foil (~100 μm), and a second was placed outside the chamber at ~320 cm from the TCC.

Both of these probes (D-dot and B-dot) give information on the time derivatives of the detected electric and magnetic fields. An appropriate numerical integration is thus required to retrieve information on the fields from the stored signals. Characteristic signals for both the electric and the magnetic fields obtained in this experimental campaign by the probes inside the chamber are reported in Figs. 14(c) and 14(d) in the time and frequency domains, respectively. Typical maximum intensities for the measured electric fields when shooting on Al targets of 2 μm thickness were ~10 kV m^{-1} peak-to-peak inside the vacuum chamber [see Fig. 14(c)], and ~100 V m^{-1} peak-to-peak outside. Typical H field values were 60 A m^{-1} inside [see Fig. 14(c)] and 1.5 A m^{-1} outside the chamber. The EMP duration was of the order of several hundreds of nanoseconds. EMPs are inversely dependent on the distance from TCC; thus, at positions closer to the interaction point, fields much higher than those detected by the internal D-dot probe are produced. These exceed the typical damage threshold (10 kV m^{-1}) for unshielded active electronic equipment.

An intensity scan, performed by changing the focusing position of the parabola at fairly constant laser pulse energy, is shown in Fig. 14(b). Here, the maximum values of the signals on the oscilloscope are expressed in volts and normalized to the laser energy. As expected, the measured maximum intensity of both electric and magnetic fields sensed both inside and outside the chamber was obtained at the best focus, corresponding to the maximum laser intensity.

These tests, conducted at laser intensities that are still lower than the future full-power output of Apollon, have been fundamental to introducing an EMP measurement platform and starting to optimize shielding and mitigation techniques and management of signal transmission. In fact, already at these laser intensities, EMPs are recognized to be serious threats to electronics inside the chamber. The Apollon upgrade to the multi-PW level will allow us to enter a regime of EMP emissions that is still unexplored and to supply data for short and energetic pulses. The general scaling obtained from experimental data reported by other existing laser facilities[9] shows that for 100 J laser pulses in the picosecond regime, EMP fields grow up to several hundreds of kV m^{-1} at ~1 m from the TCC. Thus, when Apollon runs in the multi-PW regime, we expect EMP levels to increase by more than an order of magnitude with respect to what was detected in this commissioning campaign. However, since EMP power depends also on the specific laser intensity at focus and on the target used, it is necessary to be well prepared for even more significant growths of these pulses.

IV. CONCLUSIONS AND PERSPECTIVES

The Apollon laser facility is a users' facility open to researchers worldwide. The present report details how its SFA area underwent successful commissioning. A number of diagnostics employing active detectors were subjected to tests in which they were operated over a series of shots without the need to retrieve detection materials. We demonstrated that TNSA proton beams with cutoff energies around 28 MeV could be produced from 2 to 3 μm thick Al foils, which are particularly suitable for applications such as proton radiography. The emissions of electrons, ions, and high-energy electromagnetic radiation that were recorded show good laser–target coupling and an overall performance that is highly consistent with what has been reported by similar international facilities. We showed that the laser displays very good temporal contrast characteristics and that the plasma gradient scale-length at the target front is between $\lambda_L/20$ and $\lambda_L/5$. Upcoming experimental campaigns will be carried out to test the implementation of plasma mirrors[46] in order to allow interactions in a ultra-high-contrast regime or with ultra-thin targets. The next phase will be the upgrade of the Apollon laser to 4 PW, which is scheduled for the year 2022, and which will be followed by a further upgrade to the final 10 PW level.

ACKNOWLEDGMENTS

The authors acknowledge the facility and the technical assistance of the national research infrastructure Apollon. The authors would also like to thank all teams of the laboratories that contributed to the success of the facility, i.e., all of the CILEX consortium, which was established to build Apollon. This work was supported by funding from the European Research Council (ERC) under the European Unions Horizon 2020 research and innovation program (Grant Agreement No. 787539, Project GENESIS), and by Grant No. ANR-17-CE30-0026-Pinnacle from the Agence Nationale de la Recherche. We acknowledge, in the framework of Project GENESIS, the support provided by Extreme Light Infrastructure Nuclear Physics (ELI-NP) Phase II, a project co-financed by the Romanian Government and the European Union through the European Regional Development Fund, and by the Project No. ELI-RO-2020-23, funded by IFA (Romania) to design, build, and test the neutron detectors used in this project, as well as parts of the OTR diagnostic. JIHT RAS team members are supported by the Ministry of Science and Higher Education of the Russian Federation (State Assignment No. 075-00460-21-00). The study reported here was also funded by the Russian Foundation for Basic Research, Project No. 20-02-00790. The work of the ENEA team members has been carried out within the framework of the EUROfusion Consortium and has received funding from the Euratom research and training program 2014–2018 and 2019-2020 under grant agreement No. 633053. The views and opinions expressed herein do not necessarily reflect those of the European Commission.

AUTHOR DECLARATIONS

Conflict of Interest

The authors have no conflicts to disclose.

DATA AVAILABILITY

All data needed to evaluate the conclusions in the paper are present in the paper. Experimental data are archived on servers at LULI and are available from the corresponding author upon reasonable request.

REFERENCES

[1]C. N. Danson, C. Haefner, J. Bromage, T. Butcher, J.-C. F. Chanteloup, E. A. Chowdhury, A. Galvanauskas, L. A. Gizzi, J. Hein, D. I. Hillier *et al.*, "Petawatt and exawatt class lasers worldwide," High Power Laser Sci. Eng. **7**, e54 (2019).

[2]F. Lureau, G. Matras, O. Chalus, C. Derycke, T. Morbieu, C. Radier, O. Casagrande, S. Laux, S. Ricaud, G. Rey *et al.*, "High-energy hybrid femtosecond laser system demonstrating 2 × 10 PW capability," High Power Laser Sci. Eng. **8**, e43 (2020).

[3]D. N. Papadopoulos, P. Ramirez, K. Genevrier, L. Ranc, N. Lebas, A. Pellegrina, C. Le Blanc, P. Monot, L. Martin, J. P. Zou, F. Mathieu, P. Audebert, P. Georges, and F. Druon, "High-contrast 10 fs OPCPA-based front end for multi-PW laser chains," Opt. Lett. **42**, 3530–3533 (2017).

[4]D. N. Papadopoulos, J. P. Zou, C. Le Blanc, G. Chériaux, P. Georges, F. Druon, G. Mennerat, P. Ramirez, L. Martin, A. Fréneaux *et al.*, "The Apollon 10 PW laser: Experimental and theoretical investigation of the temporal characteristics," High Power Laser Sci. Eng. **4**, e34 (2016).

[5]J. P. Zou, C. Le Blanc, D. N. Papadopoulos, G. Chériaux, P. Georges, G. Mennerat, F. Druon, L. Lecherbourg, A. Pellegrina, P. Ramirez *et al.*, "Design and current progress of the Apollon 10 PW project," High Power Laser Sci. Eng. **3**, e2 (2015).

[6]D. N. Papadopoulos, J. P. Zou, C. L. Blanc, L. Ranc, F. Druon, L. Martin, A. Fréneaux, A. Beluze, N. Lebas, M. Chabanis, C. Bonnin, J. B. Accary, B. L. Garrec, F. Mathieu, and P. Audebert, in *Conference on Lasers and Electro-Optics* (Optical Society of America, 2019), p. STu3E.4.

[7]D. N. Papadopoulos, J. P. Zou, C. L. Blanc, L. Ranc, F. Druon, L. Martin, A. Fréneaux, A. Beluze, N. Lebas, M. Chabanis, B. L. Garrec, F. Mathieu, and P. Audebert, "The Apollon laser: Commissioning results of the 1 PW beam line," in High Power Laser Science and Engineering, Suzhou, China, 12–16 April 2021.

[8]J.-L. Dubois, F. Lubrano-Lavaderci, D. Raffestin, J. Ribolzi, J. Gazave, A. Compant La Fontaine, E. d'Humières, S. Hulin, P. Nicolaï, A. Poyé, and V. T. Tikhonchuk, "Target charging in short-pulse-laser-plasma experiments," Phys. Rev. E **89**, 013102 (2014).

[9]F. Consoli, V. T. Tikhonchuk, M. Bardon, P. Bradford, D. C. Carroll, J. Cikhardt, M. Cipriani, R. J. Clarke, T. E. Cowan, C. N. Danson, R. De Angelis, M. De Marco, J.-L. Dubois, B. Etchessahar, A. L. Garcia, D. I. Hillier, A. Honsa, W. Jiang, V. Kmetik, J. Krása, Y. Li, F. Lubrano, P. McKenna, J. Metzkes-Ng, A. Poyé, I. Prencipe, P. Rączka, R. A. Smith, R. Vrana, N. C. Woolsey, E. Zemaityte, Y. Zhang, Z. Zhang, B. Zielbauer, and D. Neely, "Laser produced electromagnetic pulses: Generation, detection and mitigation," High Power Laser Sci. Eng. **8**, e22 (2020).

[10]F. Consoli, P. L. Andreoli, M. Cipriani, G. Cristofari, R. De Angelis, G. Di Giorgio, L. Duvillaret, J. Krása, D. Neely, M. Salvadori, M. Scisciò, R. A. Smith, and V. T. Tikhonchuk, "Sources and space–time distribution of the electromagnetic pulses in

experiments on inertial confinement fusion and laser–plasma acceleration," Philos. Trans. R. Soc., A **379**, 20200022 (2020).

[11]P. R. Bolton, M. Borghesi, C. Brenner, D. C. Carroll, C. De Martinis, F. Fiorini, A. Flacco, V. Floquet, J. Fuchs, P. Gallegos, D. Giove, J. S. Green, S. Green, B. Jones, D. Kirby, P. McKenna, D. Neely, F. Nuesslin, R. Prasad, S. Reinhardt, M. Roth, U. Schramm, G. G. Scott, S. Ter-Avetisyan, M. Tolley, G. Turchetti, and J. J. Wilkens, "Instrumentation for diagnostics and control of laser-accelerated proton (ion) beams," Phys. Med. **30**, 255–270 (2014).

[12]L. Ranc, C. Le Blanc, N. Lebas, L. Martin, J.-P. Zou, F. Mathieu, C. Radier, S. Ricaud, F. Druon, and D. Papadopoulos, "Improvement in the temporal contrast in the tens of ps range of the multi-PW Apollon laser front-end," Opt. Lett. **45**, 4599–4602 (2020).

[13]H. Popescu, S. D. Baton, F. Amiranoff, C. Rousseaux, M. R. Le Gloahec, J. J. Santos, L. Gremillet, M. Koenig, E. Martinolli, T. Hall, J. C. Adam, A. Heron, and D. Batani, "Subfemtosecond, coherent, relativistic, and ballistic electron bunches generated at ω_0 and $2\omega_0$ in high intensity laser-matter interaction," Phys. Plasmas **12**, 063106 (2005).

[14]A. Do, M. Briat, S. D. Baton, M. Krumrey, L. Lecherbourg, B. Loupias, F. Pérez, P. Renaudin, C. Rubbelynck, and P. Troussel, "Two-channel high-resolution quasi-monochromatic X-ray imager for Al and Ti plasma," Rev. Sci. Instrum. **89**, 113702 (2018).

[15]P. Renaudin, L. Duthoit, S. Baton, C. Blancard, A. Chaleil, P. Cossé, G. Faussurier, L. Gremillet, L. Lecherbourg, B. Loupias, and F. Perez, "Radiative cooling of an Al plasma in an Al-Ti mixture heated by an ultraintense laser pulse," High Energy Density Phys. (to be published), available at, https://hal.archives-ouvertes.fr/hal-02456723/.

[16]A. Y. Faenov, S. A. Pikuz, A. I. Erko, B. A. Bryunetkin, V. M. Dyakin, G. V. Ivanenkov, A. R. Mingaleev, T. A. Pikuz, V. M. Romanova, and T. A. Shelkovenko, "High-performance x-ray spectroscopic devices for plasma microsources investigations," Phys. Scr. **50**, 333–338 (1994).

[17]U. Andiel, K. Eidmann, P. Hakel, R. C. Mancini, G. C. Junkel-Vives, J. Abdallah, and K. Witte, "Demonstration of aluminum K-shell line shifts in isochorically heated targets driven by ultrashort laser pulses," Europhys. Lett. **60**, 861–867 (2002).

[18]M. A. Alkhimova, A. Y. Faenov, I. Y. Skobelev, T. A. Pikuz, M. Nishiuchi, H. Sakaki, A. S. Pirozhkov, A. Sagisaka, N. P. Dover, K. Kondo, K. Ogura, Y. Fukuda, H. Kiriyama, K. Nishitani, T. Miyahara, Y. Watanabe, S. A. Pikuz, M. Kando, R. Kodama, and K. Kondo, "High resolution X-ray spectra of stainless steel foils irradiated by femtosecond laser pulses with ultra-relativistic intensities," Opt. Express **25**, 29501–29511 (2017).

[19]L. Chopineau, A. Leblanc, G. Blaclard, A. Denoeud, M. Thévenet, J.-L. Vay, G. Bonnaud, P. Martin, H. Vincenti, and F. Quéré, "Identification of coupling mechanisms between ultraintense laser light and dense plasmas," Phys. Rev. X **9**, 011050 (2019).

[20]S. Kahaly, S. Monchocé, H. Vincenti, T. Dzelzainis, B. Dromey, M. Zepf, P. Martin, and F. Quéré, "Direct observation of density-gradient effects in harmonic generation from plasma mirrors," Phys. Rev. Lett. **110**, 175001 (2013).

[21]Y. I. Salamin, S. Hu, K. Z. Hatsagortsyan, and C. H. Keitel, "Relativistic high-power laser–matter interactions," Phys. Rep. **427**, 41–155 (2006).

[22]A. Lévy, T. Ceccotti, P. D'Oliveira, F. Réau, M. Perdrix, F. Quéré, P. Monot, M. Bougeard, H. Lagadec, P. Martin, J.-P. Geindre, and P. Audebert, "Double plasma mirror for ultrahigh temporal contrast ultraintense laser pulses," Opt. Lett. **32**, 310–312 (2007).

[23]R. A. Snavely, M. H. Key, S. P. Hatchett, T. E. Cowan, M. Roth, T. W. Phillips, M. A. Stoyer, E. A. Henry, T. C. Sangster, M. S. Singh, S. C. Wilks, A. MacKinnon, A. Offenberger, D. M. Pennington, K. Yasuike, A. B. Langdon, B. F. Lasinski, J. Johnson, M. D. Perry, and E. M. Campbell, "Intense high-energy proton beams from petawatt-laser irradiation of solids," Phys. Rev. Lett. **85**, 2945–2948 (2000).

[24]J. J. Thomson, "XXVI. Rays of positive electricity," London, Edinburgh Dublin Philos. Mag. J. Sci. **21**, 225–249 (1911).

[25]J. Fuchs, P. Antici, E. d'Humières, E. Lefebvre, M. Borghesi, E. Brambrink, C. A. Cecchetti, M. Kaluza, V. Malka, M. Manclossi, S. Meyroneinc, P. Mora, J. Schreiber, T. Toncian, H. Pépin, and P. Audebert, "Laser-driven proton scaling laws and new paths towards energy increase," Nat. Phys. **2**, 48–54 (2006).

[26]T. Ceccotti, A. Lévy, H. Popescu, F. Réau, P. D'Oliveira, P. Monot, J. P. Geindre, E. Lefebvre, and P. Martin, "Proton acceleration with high-intensity ultrahigh-contrast laser pulses," Phys. Rev. Lett. **99**, 185002 (2007).

[27]A. Soloviev, K. Burdonov, S. N. Chen, A. Eremeev, A. Korzhimanov, G. V. Pokrovskiy, T. A. Pikuz, G. Revet, A. Sladkov, V. Ginzburg, E. Khazanov, A. Kuzmin, R. Osmanov, I. Shaikin, A. Shaykin, I. Yakovlev, S. Pikuz, M. Starodubtsev, and J. Fuchs, "Experimental evidence for short-pulse laser heating of solid-density target to high bulk temperatures," Sci. Rep. **7**, 12144 (2017).

[28]S. C. Wilks, A. B. Langdon, T. E. Cowan, M. Roth, M. Singh, S. Hatchett, M. H. Key, D. Pennington, A. MacKinnon, and R. A. Snavely, "Energetic proton generation in ultra-intense laser–solid interactions," Phys. Plasmas **8**, 542–549 (2001).

[29]H. Daido, M. Nishiuchi, and A. S. Pirozhkov, "Review of laser-driven ion sources and their applications," Rep. Prog. Phys. **75**, 056401 (2012).

[30]A. Macchi, M. Borghesi, and M. Passoni, "Ion acceleration by superintense laser-plasma interaction," Rev. Mod. Phys. **85**, 751–793 (2013).

[31]M. Allen, P. K. Patel, A. Mackinnon, D. Price, S. Wilks, E. Morse, "Direct experimental evidence of back-surface ion acceleration from laser-irradiated gold foils," Phys. Rev. Lett. **93**, 265004 (2004).

[32]J. C. Adam, A. Héron, and G. Laval, "Dispersion and transport of energetic particles due to the interaction of intense laser pulses with overdense plasmas," Phys. Rev. Lett. **97**, 205006 (2006).

[33]J. S. Green, V. M. Ovchinnikov, R. G. Evans, K. U. Akli, H. Azechi, F. N. Beg, C. Bellei, R. R. Freeman, H. Habara, R. Heathcote, M. H. Key, J. A. King, K. L. Lancaster, N. C. Lopes, T. Ma, A. J. MacKinnon, K. Markey, A. McPhee, Z. Najmudin, P. Nilson, R. Onofrei, R. Stephens, K. Takeda, K. A. Tanaka, W. Theobald, T. Tanimoto, J. Waugh, L. Van Woerkom, N. C. Woolsey, M. Zepf, J. R. Davies, and P. A. Norreys, "Effect of laser intensity on fast-electron-beam divergence in solid-density plasmas," Phys. Rev. Lett. **100**, 015003 (2008).

[34]J. Fuchs, C. A. Cecchetti, M. Borghesi, T. Grismayer, E. d'Humières, P. Antici, S. Atzeni, P. Mora, A. Pipahl, L. Romagnani, A. Schiavi, Y. Sentoku, T. Toncian, P. Audebert, and O. Willi, "Laser-foil acceleration of high-energy protons in small-scale plasma gradients," Phys. Rev. Lett. **99**, 015002 (2007).

[35]P. Wang, G. Qi, Z. Pan, D. Kong, Y. Shou, J. Liu, Z. Cao, Z. Mei, S. Xu, Z. Liu *et al.*, "Fabrication of large-area uniform carbon nanotube foams as near-critical-density targets for laser–plasma experiments," High Power Laser Sci. Eng. **9**, e29 (2021).

[36]S. N. Chen, M. Gauthier, M. Bazalova-Carter, S. Bolanos, S. Glenzer, R. Riquier, G. Revet, P. Antici, A. Morabito, A. Propp, M. Starodubtsev, and J. Fuchs, "Absolute dosimetric characterization of Gafchromic EBT3 and HDv2 films using commercial flat-bed scanners and evaluation of the scanner response function variability," Rev. Sci. Instrum. **87**, 073301 (2016).

[37]V. Lelasseux and J. Fuchs, "Modelling energy deposition in TR image plate detectors for various ion types," J. Instrum. **15**(04), P04002 (2020).

[38]K. Ogura, M. Nishiuchi, A. S. Pirozhkov, T. Tanimoto, A. Sagisaka, T. Z. Esirkepov, M. Kando, T. Shizuma, T. Hayakawa, H. Kiriyama, T. Shimomura, S. Kondo, S. Kanazawa, Y. Nakai, H. Sasao, F. Sasao, Y. Fukuda, H. Sakaki, M. Kanasaki, A. Yogo, S. V. Bulanov, P. R. Bolton, and K. Kondo, "Proton acceleration to 40 MeV using a high intensity, high contrast optical parametric chirped-pulse amplification Ti:sapphire hybrid laser system," Opt. Lett. **37**, 2868–2870 (2012).

[39]F. Wagner, O. Deppert, C. Brabetz, P. Fiala, A. Kleinschmidt, P. Poth, V. A. Schanz, A. Tebartz, B. Zielbauer, M. Roth, T. Stöhlker, and V. Bagnoud, "Maximum proton energy above 85 MeV from the relativistic interaction of laser pulses with micrometer thick CH_2 targets," Phys. Rev. Lett. **116**, 205002 (2016).

[40]H. Chen, N. L. Back, T. Bartal, F. N. Beg, D. C. Eder, A. J. Link, A. G. MacPhee, Y. Ping, P. M. Song, A. Throop, and L. Van Woerkom, "Absolute calibration of image plates for electrons at energy between 100 keV and 4 MeV," Rev. Sci. Instrum. **79**, 033301 (2008).

[41]A. Alejo, H. Ahmed, A. Green, S. R. Mirfayzi, M. Borghesi, and S. Kar, "Recent advances in laser-driven neutron sources," Nuovo Cimento **38**, 188 (2015).

[42]S. R. Mirfayzi, S. Kar, H. Ahmed, A. G. Krygier, A. Green, A. Alejo, R. Clarke, R. R. Freeman, J. Fuchs, D. Jung, A. Kleinschmidt, J. T. Morrison, Z. Najmudin, H. Nakamura, P. Norreys, M. Oliver, M. Roth, L. Vassura, M. Zepf, and M. Borghesi, "Calibration of time of flight detectors using laser-driven neutron source," Rev. Sci. Instrum. **86**, 073308 (2015).

[43]Electric Field Sensors, D-Dot free field-radial output (R), Data Sheet Prodyn Technologies; accessed 22 July 2021.

[44]Radiation hardened B-Dot Sensor–Model RB-230(R), Data Sheet Prodyn Technologies; accessed 22 July 2021.

[45]P. Baluns, Data Sheet Prodyn Technologies; accessed 22 July 2021.

[46]C. Thaury, F. Quéré, J.-P. Geindre, A. Levy, T. Ceccotti, P. Monot, M. Bougeard, F. Réau, P. d'Oliveira, P. Audebert, R. Marjoribanks, and P. Martin, "Plasma mirrors for ultrahigh-intensity optics," Nat. Phys. **3**, 424–429 (2007).